



Geometrical, microstructural and mechanical characterization of pulse laser welded thin sheet 5052-H32 aluminium alloy for aerospace applications

T. E. ABIOYE^{1,2}, H. ZUHAILAWATI¹, S. AIZAD¹, A. S. ANASYIDA¹

1. Structural Materials Niche Area, School of Materials and Mineral Resources Engineering, Engineering Campus, Universiti Sains Malaysia, 14300 Nibong Tebal, Penang, Malaysia;

2. Industrial and Production Engineering Department, School of Engineering and Engineering Technology, Federal University of Technology Akure, PMB 704, Akure, Ondo State, Nigeria

Received 16 July 2018; accepted 14 January 2019

Abstract: Pulse laser welding of 0.6 mm-thick AA5052-H32 was performed to determine the optimum set of parameters including laser pulse current, pulse frequency and pulse duration that meets the AWS D17.1 specifications for aerospace industry. The microstructure and mechanical properties of the weldments were also investigated. Relationships between the parameters and weld bead geometry were found. High quality weld joints without solidification crack that met AWS D17.1 requirements were obtained at (I) high pulse energy (25 J) and high average peak power (4.2 kW) and (II) low pulse energy (17.6 J) and low average peak power (2.8 kW). The weld joint formed at lower heat energy input exhibited finer dendritic grain structure. Mg vapourisation and hard phase compound ($Al_{0.5}Fe_3Si_{0.5}$) formation decreased in the weld joint formed at lower heat energy input. Consequently, the tensile strength of the weldment formed at lower heat energy input (168 MPa) is by a factor of 1.15 higher but showed ~29% decrease in hardness (111 HV_{0.1}) at the joint when being compared with the weldment formed at higher heat energy input. Appropriate parameters selection is critical to obtaining 0.6 mm-thick AA5052-H32 pulse laser weld joints that meet AWS D17.1 requirements for aircraft structures.

Key words: pulse laser welding; aluminium alloy; thin sheet; microstructure; mechanical properties; solidification cracking; intermetallic compound

1 Introduction

Laser welding has been established as an advanced technique for joining metals such as steels [1], titanium alloys [2] and magnesium alloys [3,4]. This is due to the advantages it offers over the conventional arc welding techniques including shielded metal arc, gas metal arc, gas tungsten arc welding, etc. Due to the focusability of the laser beam, laser welding produces high concentrated energy density heat source resulting in minimal distortion, strong weld joint [5] and low dilution in case of dissimilar metal joints [6]. Other advantages of the technique/process include high processing speed, flexibility, precision and ease of automating the process [7]. Laser welding is a non-contact process in which a beam of coherent, monochromatic light, acting as the heat energy source, is focused to a small spot on the abutting surfaces of the parts being joined. The heat

energy melts the surfaces creating a melt pool which solidifies as the laser beam moves over the parts. Due to the controllable heat energy input, the technique has generally been adopted as a welding method for aluminium alloys [8,9]. Although laser welding operates either in continuous or pulse mode, the latter is expected to give a more precise heat control which produces reduced heat affected zone (HAZ) and residual stresses [10].

Generally, aluminium alloys are increasingly being used for the fabrication of components for several engineering applications. This is due to their excellent combinations of favourable properties including lightweight, high corrosion resistance, easiness with design (high malleability), etc. For example, AA series 2000, 7000 and Al–Li are materials of choice for making different aircraft parts where damage tolerance, high strength, high stiffness combined with light weight and low cost are highly required [11]. AA series 5000,

especially AA 5052, is known for high corrosion resistance in marine environments, high thermal conductivity, good strength, good formability and weldability [12]. Specifically, AA series 5052 is increasingly replacing steels in marine and automotive industries for making structural parts.

Generally, joining aluminium alloys via laser welding is often difficult because of the material's high reflectivity (leading to absorption of some fraction of the incident radiation), high thermal conductivity (provoking a fast heat transfer in the welding piece that limits the concentration of energy in the weld pool), and low viscosity (restricting the growth of the weld pool before solidification of aluminium thin sheet) [13]. Therefore, it is important to have high laser heat energy supply that gives a minimum absorbed energy sufficient for complete melting of the alloys. CHEN and MOLIAN [14] have shown that this is achievable via conduction mode or deep penetration mode. The latter is commonly used because of the benefits it offers including better energy coupling, higher welding speed, and thicker-section welding capability. However, the conduction mode is often preferred for welding aluminium thin sheet because of its ability to minimise distortion, prevent loss of alloying elements and produce fine grain structures through rapid solidification [15]. Another issue of concern with the welding aluminium alloy is the high propensity for cracking in the weld region.

In the past, extensive work has been done in obtaining high quality AA 5052 laser welds free of defects like solidification cracking, and porosity. EL-BATAHGY and KUTSUNA [16] reported that the problem of solidification cracking in laser welding of aluminium alloys has been solved through the introduction of suitable filler metals by decreasing the stress concentration in the weld zone through improvement of the weld pool profile. Also, the filler metal must contain high alloying elements (e.g., Mg and Si) so as to reduce the solidification range of the weld metal [17]. Prediction of solidification cracking in pulse laser welding of aluminium alloys has been researched by SHEIKHI et al [18]. It was found that welding with suitable ramping down of laser pulse prevents crack initiation in the weld joint.

Partial penetration during the autogenous laser welding of AA 5052-H32 was studied by ABATAKI et al [19]. It was established that pore formation is a result of the shielding gas entrapment caused by the collapse of the keyholes. However, using helium gas as the shielding gas at low welding speed could mitigate pores formation during the process. BUNAZIV et al [20] investigated the effects of the welding parameters and shielding gas composition on the 5 mm-thick AA 5083 weld quality using fiber laser-MIG hybrid technique. It

was revealed that the addition of expensive helium to shielding gas has not much significant effect on the porosity decrease, process stability and weld mechanical properties as the selected welding parameters. Due to the high reflectivity, it has been discovered that aluminium alloys absorb more laser heat energy at lower wavelength [20]. Consequently, Nd-YAG laser ($\lambda=1.06$ nm), compared with CO₂ laser ($\lambda=10.06$ nm), is more suitable for welding aluminium alloys.

Optimisation of process parameters for obtaining excellent weld qualities has been done for different material systems. The suitable parametric combinations for different aluminium alloys thickness have been established. EL-BATAHGY and KUTSUNA [16] established that high quality weld with a full penetration is attainable at a welding speed of 5 m/min, CO₂ laser power of 4 kW for 2 mm-thick joint and welding speed of 6 m/min and CO₂ laser power of 5 kW for a 3 mm-thick joint of AA 5052 and AA 5083. The weld metal surfaces were positioned 1.5 mm above the laser beam focus. Fibre laser power of 15 and 20 kW was respectively found suitable for welding speeds of 1.8 and 2.4 m/min for the welding of 20 mm-thick S 355 structural steel using a focal point of about 7.5 mm [21]. An optimal processing condition has been established by SU et al [22] for a 2 mm AA 6061-T6 aluminium alloy thick plate butt welding using a 6 kW TruDisk6002 laser with wavelength of 1.06 nm and laser spot diameter of 2 mm. A high quality weld with a smooth and continuous bead was obtained at a laser power of 2.3 kW and welding speed of 3 m/mm after preheating the workpiece. A research on the elimination of solidification cracking during welding of 2.5 mm-thick AA 6013 aluminium alloy using varying parameters has been done by WANG et al [23]. It was found that solidification cracking disappears at a welding speed of 3.3 m/mm when the fiber laser power was set at 3.3 kW with a spot diameter of 0.8 mm. Till date, the appropriate laser welding parameters for obtaining high quality joints for thin sheet (0.6 mm thick) AA series 5000 using either pulse or continuous wave laser have not been established. Thin sheet AA 5052-H32 is now finding applications in aerospace industry for the fabrication of light-weight and low cost TV-screen frame at the back of passenger's seat in the aeroplane. The welding/joining of the thin aluminium alloy sheet must meet the specification given by the aerospace industry.

In this work, pulse laser welding of 0.6 mm-thick AA 5052-H32 alloy was done at varying parametric combinations using L9 Taguchi orthogonal array method. The profiles and macrostructures of the weld joints were evaluated for defects and then compared with the aerospace space specification (AWS D17.1). The effects of the pulse laser welding parameters such as pulse

energy and average peak power on the microstructure, hardness and tensile strength of the weldments were also investigated.

2 Experimental

2.1 Materials

An aluminium plate AA 5052-H32 with thickness of 0.6 mm supplied by Gulf Aluminium Rolling Mill Co., Bahrain was used as the base metal while the filler wire utilised is aluminium ER5356 with thickness of 0.6 mm. The aluminium plate was machined into dimension of 200 mm × 100 mm × 0.6 mm with butt angle of 60° at the edge of plates. The chemical compositions of the base metal and filler metal as revealed from the energy dispersive X-ray (EDX) analysis are presented in Table 1. The shielding gas used is Argon. Prior to the welding and the chemical analysis, the edges and surfaces of the plates and filler wire were grit blasted so as improve laser absorptivity. Thereafter, the plates were thoroughly cleaned with acetone so as to remove all form of impurities.

2.2 Laser welding process

Pulsed laser welding with butt joint configuration was performed using the nine (9) parametric combinations presented in Table 2. The combinations of

parameters were obtained using L9 Taguchi orthogonal array after some trial experiments were done. The maximum and minimum values for each utilised parameter show the range within which continuous welds without visible pores were obtained (based on visual observation) during trial experiments.

The entire pulsed laser welding was carried out using Nd:YAG laser operating at 1064 nm wavelength with an average power of 200 W. The laser beam spot diameter was adjusted to be 0.8 mm. The entire welding took place in an argon filled environment (10 L/min) so as to prevent weld pool interaction with the atmosphere.

Thereafter, samples used for microstructure examination, hardness measurement and tensile test were cut out, across the weldment, using laser cutting machine. The samples were cut around the middle of the weldments because it is believed that it takes few seconds before the stability is reached while welding. The pulse energy (E_p) and average peak power (P_{AP}) in Table 2 were determined using Eqs. (1) and (2):

$$E_p = \frac{P_A}{f} \quad (1)$$

$$P_{AP} = \frac{E_p}{t} \quad (2)$$

where P_A , f and t are average laser power, pulse frequency and pulse duration, respectively.

Table 1 Chemical compositions of base metal and filler wire (wt.%)

Material	Al	Mg	Si	Ti	Cr	Mn	Fe	Ni	Cu	Zn	Ga
AA 5052-H32	96.66	2.62	0.29	0.02	0.18	0.06	0.15	0.01	0.02	0.01	0.01
ER 5356 aluminium filler wire	94.65	4.87	0.22	0.07	0.01	0.05	0.11	–	0.02	0.01	–

Table 2 Parameters utilised for pulsed laser welding

Sample No.	Input parameter					Calculated parameter	
	Pulse current, I/A	Pulse frequency, f/Hz	Pulse duration, t/ms	Laser beam diameter, d/mm	Welding speed, V/(mm·min ⁻¹)	Pulse energy, E_p /J	Average peak power, P_{AP} /kW
1	215	8	5	0.8	200	25.0	5.0
2	215	10	6	0.8	200	20.0	3.3
3	215	12	7	0.8	200	16.7	2.4
4	235	8	6	0.8	200	25.0	4.2
5	235	10	7	0.8	200	20.0	2.9
6	235	12	5	0.8	200	16.7	3.3
7	255	8	7	0.8	200	25.0	3.6
8	255	10	5	0.8	200	20.0	4.0
9	255	12	6	0.8	200	16.7	2.8

Average laser power: 200 W

2.3 Macrostructure and microstructure examination

Prior to the macrostructure and microstructural examinations, the transversely cross-sectioned weld samples were cleaned, ground and polished to 1 μm surface finish. Thereafter, the polished samples were etched in 0.5% HF solution for about 10–15 s. First, the samples were viewed and images were taken at varying magnification using Stereo-zoom optical microscope. The weld joints profiles were determined from the captured optical images and then compared with the aerospace specification (AWS D17.1). The microstructure of the HAZ, weld (fusion) zone and base metal were determined using a combination of scanning electron microscopy, energy dispersive X-ray spectroscopy and X-ray diffractometry.

2.4 Weld bead width optimisation

In order to study the main effects of the pulsed laser parameters on the weld bead width, signal-to-noise (S/N) ratio from the weld width value obtained for each parametric combination was calculated. A higher-is-better (HB) criterion was selected so as to maximise the response [24]:

$$S/N = -10 \lg \frac{1}{n} \sum_{i=1}^n \left(\frac{1}{y_i^2} \right) \quad (3)$$

where y is the weld bead width for each parametric combination and n is the number of trials ($n=3$). Thereafter, the main effect of each parameter and the optimal setting were determined from the calculated S/N ratios.

2.5 Mechanical test

The Vickers micro-hardness of the weldments was taken across the weldments from the base metal through the HAZ to the weld joint. A test load of 0.1 kg was used for about 15 s. A spacing of about 0.15 mm was allowed in-between the successive indentations so as to ensure fair and accurate results. The tensile test was performed using Instron Universal Testing Machine at a constant cross-head speed of 1 mm/min. Three test samples from each of the weldments were prepared and tested following ASTM E8M–13. The average of three measurements gave the tensile strength of each weldment.

2.6 Fracture surface analysis

After the tensile test, samples were cut near the fracture region so as to carry out fracture surface analysis. The fracture surfaces were cleaned, etched and examined under a TM3000 Hitachi Tabletop Microscope SEM, with a voltage of 5 kV.

3 Results and discussion

3.1 Macrostructure evaluation and weld bead optimisation

Optical macrographs showing the transversely cross-sectioned area of the weldments are presented in Fig. 1. Apparently, the weld bead width varies with the pulsed laser parameters. Also, it is obvious that solidification cracking occurred in the weld zone of nearly all the weldments except for samples 4 and 9. According to CAO et al [4], improper selection of process parameters which often produce irregular weld shapes has been identified as one of the causes of solidification cracking. One of the means of preventing this occurrence is proper selection of parameters that give weld joint of wider width (i.e. relatively high aspect ratio). In this work, full weld penetration was achieved in nearly all weldments, as shown in Fig. 1. Therefore, high aspect ratio (width-to-depth ratio) will be achieved with larger weld width.

Table 3 presents the S/N ratio for each parametric combination and the main effects of each parameter on the weld width are shown in Fig. 2. As shown in Table 2, the weld bead width, for all the nine experimental runs, ranged between 0.81 and 1.22 mm.

Figure 2 revealed that the weld bead width increased with the increase in pulse current and pulse frequency; however, the width declined with the increase in pulse duration. These variations can be explained by defining the average peak power density (APPD, D_{APP}) and heat energy input (H), as illustrated in Eqs. (4) and (5) [10]:

$$D_{APP} = \frac{4P_{AP}}{\pi d^2} \quad (4)$$

$$H = \frac{E_p \cdot f}{V} \quad (5)$$

where d and V denote laser beam diameter and welding speed, respectively.

As previously defined in Eq. (2), the average peak power (P_{AP}) has an indirect relationship with the pulse duration (t). Therefore, reducing the pulse duration increases the P_{AP} . Since the laser beam diameter was constant throughout the experiments, APPD increased with decreasing the pulse duration (see Eq. (4)). With higher APPD, more heat energy is available in the weld zone (i.e., fusion zone) causing increased melting of the base and filler metals. Also, increasing the APPD increases the energy intensity in the weld pool. This is believed to have improved the fluidity of the weld pool resulting in the spreading of the pool beyond the laser

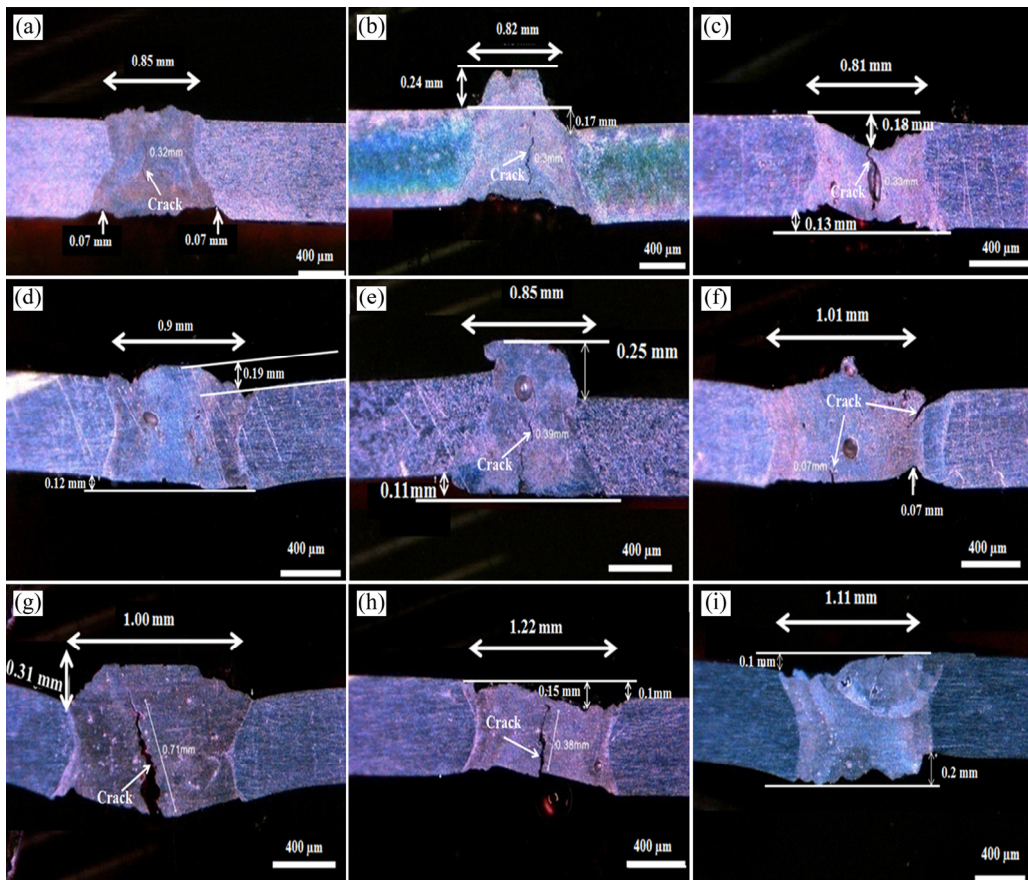


Fig. 1 Optical macrographs showing weld joint profile and macrostructure at varying parameters: (a) Sample 1: $I=215$ A, $f=8$ Hz, $t=5$ ms; (b) Sample 2: $I=215$ A, $f=10$ Hz, $t=6$ ms; (c) Sample 3: $I=215$ A, $f=12$ Hz, $t=7$ ms; (d) Sample 4: $I=235$ A, $f=8$ Hz, $t=6$ ms; (e) Sample 5: $I=235$ A, $f=10$ Hz, $t=7$ ms; (f) Sample 6: $I=235$ A, $f=12$ Hz, $t=5$ ms; (g) Sample 7: $I=255$ A, $f=8$ Hz, $t=7$ ms; (h) Sample 8: $I=255$ A, $f=10$ Hz, $t=5$ ms; (i) Sample 9: $I=255$ A, $f=12$ Hz, $t=6$ ms

Table 3 S/N ratios for weld bead width

Sample No.	Pulse current		Pulse frequency		Pulse duration		Average weld joint width/mm	SSQ	MSSQ	S/N ratio
	Level	Value/A	Level	Value/Hz	Level	Value/ms				
1	1	215	1	8	1	5	0.85	1.384	0.461	3.36
2	1	215	2	10	2	6	0.82	1.487	0.496	3.05
3	1	215	3	12	3	7	0.81	1.524	0.508	2.94
4	2	235	1	8	2	6	0.90	1.235	0.412	3.86
5	2	235	2	10	3	7	0.85	1.384	0.461	3.36
6	2	235	3	12	1	5	1.01	0.980	0.327	4.86
7	3	255	1	8	3	7	1.00	1.000	0.333	4.77
8	3	255	2	10	1	5	1.22	0.672	0.224	6.50
9	3	255	3	12	2	6	1.11	0.812	0.271	5.68

SSQ: Sum of square reciprocals; MSSQ: Mean of sum of square reciprocals

beam area. Consequently, wider weld joint was produced after solidification. This finding is in consistence with the result of TZENG [25] during pulsed Nd:YAG laser seam-welding of bare steel sheet. The slight increase in the weld width with increased frequency can be explained with the fact that at constant pulse energy, a rise in frequency enhances the average laser power and the heat energy input (see Eq. (5)). Also, pulse current in

this work is synonymous to laser power. Therefore, increasing the pulse current definitely increases the average laser power (P_A), and hence, the heat energy input (i.e. $H=P_A/V$). As the heat energy input increased, there was more melting of the base and filler metals. As explained previously, the result was wider weld bead width after solidification. A further analysis of the main effect plot in Fig. 2 shows the optimal setting for

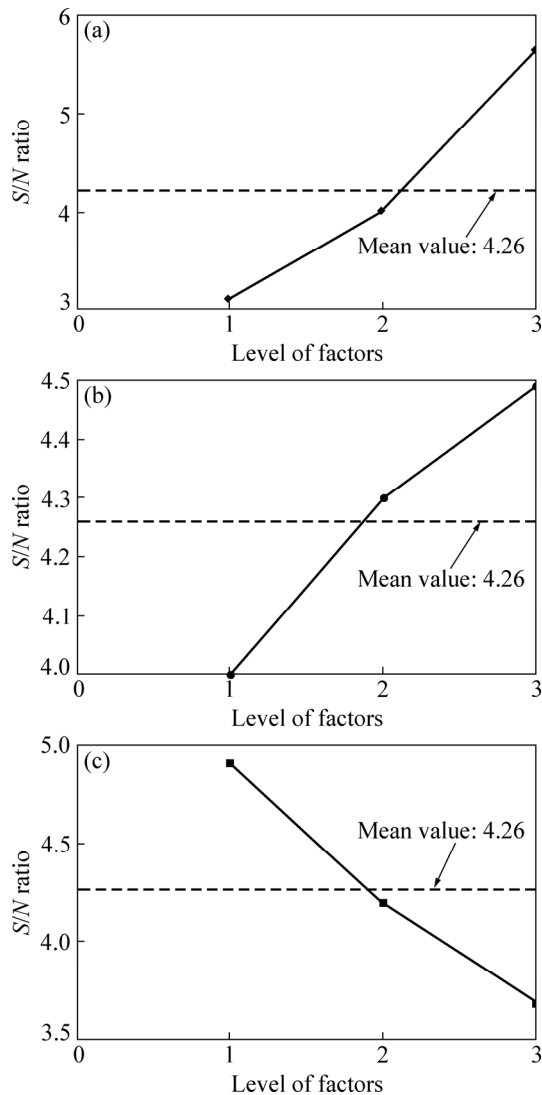


Fig. 2 Main effects of pulse laser parameters on weld bead width: (a) Pulse current; (b) Pulse frequency; (c) Pulse duration

obtaining optimum weld bead width, and hence, optimum aspect ratio for pulse laser welding of 0.6 mm-thick AA 5052-H32. This was found at Level 3 of pulse current (255 A), Level 3 of pulse frequency (12 Hz) and Level 1 of pulse duration (5 ms) based on higher-is-better criteria.

3.2 Solidification cracking

Despite the fact that all the welds exhibited sufficiently large weld width and high aspect ratio, the presence of cracks along the weld centreline of some of the samples is an indication that solidification cracking was caused by other factors. Large solidification temperature range which is often caused by the presence of trace amount of alloying elements such as Si and Mg and some impurities in pure aluminium has also been identified as a major factor initiating cracks in weld zones [26]. However, it has been revealed that the cracks

disappear by balancing the alloying elements composition in the weld zone through the selection of appropriate filler metal. However, the crack occurrence in the weld zone of some of the produced weldments could have been caused by inappropriate combination of parameters giving a misbalance between the average peak power and pulse energy.

For examples, sample 1 was welded at the lowest values of pulse frequency (8 Hz) and pulse duration (5 ms) giving the highest E_p (25 J) and P_{AP} (5 kW), as shown in Table 1. The high P_{AP} and E_p used may have caused extreme melting of the base metal resulting in high dilution. Also, significant vaporization of volatile alloying elements (e.g., Mg) could have occurred. This often results in pores formation and eventually initiates crack within the weld zone. Sample 3 was welded at the highest values of pulse frequency (12 Hz) and pulse duration (7 ms) giving the lowest values of E_p (16.7 J) and P_{AP} (2.4 kW). A critical look at the weld joint geometry (see Fig. 1(c)) revealed that there is a face under-fill of about 0.18 mm and a concave surface was noticed at the top of weld joint. This is due to the lack of sufficient energy required for faster melting of the metals. As explained by KOU [27], concave surface makes the outer surface of the joint stressed during solidification, initiating crack along the centreline of the weld joint. However, weld joints with outer surface convex are less susceptible to cracking because, with this shape, most of the developed stresses are offset towards the edges of the joint. Excessive convexity, as almost found in samples 2 and 5, can retain and produce stress concentrations, thus inducing cracking within weld joint.

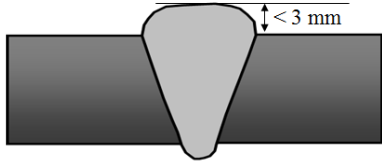
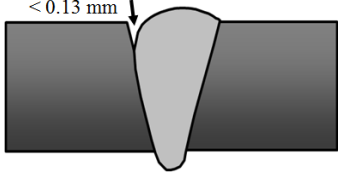
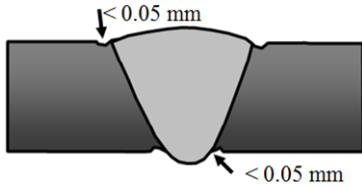
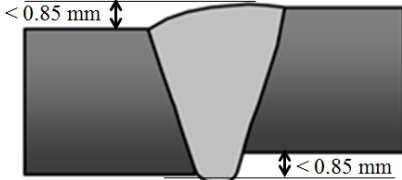
In this work, the parametric combination utilised for producing samples 4 and 9 are adjudged to be appropriate for high quality welding of 0.6 mm-thick AA 5052-H3 alloy because the welds are free of solidification cracking and their geometry met the AWS D17.1 (aerospace industry) specification, as presented in Table 4. For example, sample 4 was welded at a low frequency of 8 Hz and intermediate pulse length of 6 ms giving E_p and P_{AP} of 25 J and 4.2 kW, respectively. Each of the weld joints was analysed based on the aerospace industry specifications, as presented in Table 4. Only samples 4 and 9 fulfill the minimum criteria required in AWS D17.1. Consequently, the utilised processing parameters for making these joints (samples 4 and 9) are found appropriate for pulse laser welding of 0.6 mm-thick AA 5052-H3 alloy for the aerospace application.

3.3 Microstructure examination

3.3.1 Optical microscopy analysis

The microstructures of the two weld samples (4 and 9) formed at the appropriate parameters were examined. As shown in Fig. 3, the microstructures of two samples

Table 4 Accepted weld samples compared with AWS D17.1 (aerospace industry) specification

Acceptance criteria as per AWS D17.1	Illustration	Sample 4	Sample 9
No major crack shall be formed	–	No crack	No crack
Weld height shall not exceed 3 mm		0.19 mm	0.1 mm
Maximum face or root under fill: 0.13 mm		None	None
Maximum size of undercut: 0.05 mm		None	None
Maximum mismatch between joint: 0.85 mm		0.12 mm	0.2 mm

are categorically divided into the base metal, partially melted base metal and fusion zone. The base metal, as shown in Fig. 3, contains some pores which are believed to be due to surface contamination. The fusion zone is characterised with dendritic grain structure which is cellular at the core and columnar at the boundary. At the solid–liquid interface (i.e., at the boundary of the fusion zone), there is an evolution of columnar dendrites growing nearly perpendicularly to the base metal (see Figs. 3(b) and (e)). This is an indication that the partially melted base metal (i.e., HAZ) acts as heterogeneous nucleation sites for the evolution of the columnar dendritic structure at the interface (i.e., the fusion zone boundary). The nearly perpendicular growth of the columnar dendrites is along the heat flux direction because the heat is mainly conducted from the fusion zone to the base metal which acts as the heat sink. At the fusion core, the grain structure transits to finer but cellular dendritic structure. Compared with the microstructure (fusion zone) of the weld sample 4 formed at higher pulse energy (25 J) and higher average peak power (4.2 kW), the microstructure of the weld sample 9 ($E_p=16.7$ J, $P_{Ap}=2.8$ kW) appears to be relatively finer.

The change in the microstructure between the base metal and the fusion zone, and between the two weld samples can be attributed to the different energy input and cooling rates occurring at different positions of the weldments. According to ABIOYE et al [28], the temperature gradient (G , K/m) and solidification front rate (R , m/s) determine the microstructure of solid parts formed through heating process. The ratio G/R determines the mode of solidification while $G \cdot R$ governs the size of the grain structure formed. G depends on the temperature difference during solidification while R is a function of the cooling rate. The four solidification modes are planar, cellular dendrite, columnar dendrite and equiaxed dendrite. According to the theory of constitutional supercooling, a planar solid/liquid interface is stable at the steady state provided the condition expressed in Eq. (6) is satisfied:

$$\frac{G}{R} \geq \frac{\Delta T}{D_L} \quad (6)$$

where ΔT is the freezing range and D_L is the diffusion coefficient of the process material.

The evolution of columnar dendrite at the solid–liquid interface (i.e., boundary of the fusion zone) shows

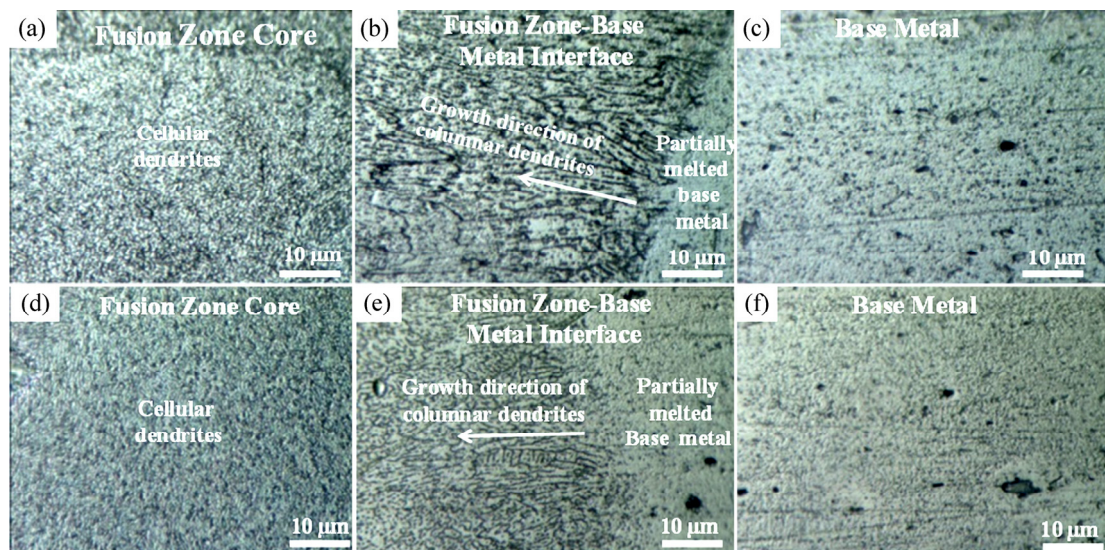


Fig. 3 Optical micrographs showing microstructures of base metal and fusion zone for pulse laser weld sample 4 (a–c) and sample 9 (d–f)

that the condition was not fulfilled. This was traced to the high thermal conductivity of the aluminium alloy (ranging 120–180 W/(m·K)) which enhanced the heat energy transfer from the weld pool (i.e., fusion zone) to the base metal [14]. Hence, cooling rate was enhanced at the interface [14]. This shows that the heat energy was quickly conducted away from the fusion zone to the base metal. As a result, solidification rate R was high such that the ratio G/R was smaller and the theory of constitutional supercooling was not fulfilled. Hence, columnar dendrite was formed. The core of the fusion zone was the hottest region in the weld pool because of its direct interaction with the laser beam. Therefore, the temperature at the core was very high compared with boundary and the base metal. This would have resulted in high temperature gradient G . However, due to high thermal conductivity of the aluminium alloy and high flow rate of the shielding gas, the cooling rate was adjudged to be faster in the core because cooling now took place mostly via conduction and convection modes. Since cooling rate is directly related to solidification growth rate (R), R will be high. Consequently, the ratio G/R was not high enough to fulfill the condition for constitutional supercooling and not low enough to form columnar dendrites. Hence, cellular dendrite solidification mode was formed in the fusion zone core. The finer grain structure found in the core of the fusion zone compared with the boundary was caused by high G and high R in the core. The value of $G \cdot R$ in the fusion zone core was larger than that of the boundary. The microstructure of the sample 9 formed at lower E_p and P_{AP} is finer because the heat energy input under this condition is lower and cooling will be rapid, and hence, finer grain structure was observed.

3.3.2 SEM/EDX analysis

Back scattered electron (BSE) images, at varying magnification, of the weld sample 4 are presented in Fig. 4. Similar to the weld sample 9, the SEM/BSE micrographs revealed the presence of two distinct phases in the fusion zone. As clearly shown in Fig. 4(c), the white contrast angular phase marked ‘A’ is randomly dispersed within the continuous dark phase spotted ‘B’. Elemental composition (EDX point analysis) of the phases was carried out at different points and the results which are average of three measurements are presented in Table 5. It was found that the white contrast angular phase marked ‘A’ contains Al (79.6 wt.%) with significant presence of Fe (19.24 wt.%) and trace amounts of other alloying elements such as Si, Mg, Ni and Cr. The continuous dark phase ‘B’ is richer in Al (97.7 wt.%) with the presence of about 2.3 wt.% Mg.

Moreover, EDX analysis (400 μm × 400 μm area scan analysis) was conducted at the core and two flanks of the fusion zone of two samples, as described in Fig. 4(a). The results, as shown in Table 6, revealed a reduction in the amount of Mg in the fusion zone as compared with the base metal and filler metal. As shown in Table 1, Mg composition in the base and filler metals are 2.62 and 4.87 wt.%, respectively. A lower value of 2.02 wt.% obtained for Mg content in the fusion zone of the sample 4 could have been due to dilution or

Table 5 Chemical composition of phases observed in fusion zone (wt.%)

Phase	Al	Mg	Si	Cr	Fe	Ni
A	79.6	0.32	0.34	0.28	19.24	0.22
B	97.7	2.3	–	–	–	–

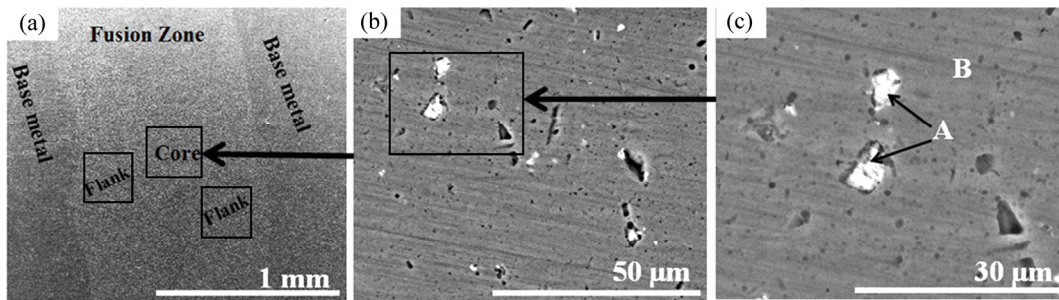


Fig. 4 SEM images showing phases present in fusion zone of pulsed laser AA 5052-H32 weldments

Table 6 Chemical composition of fusion zone of two selected samples

Sample No.	Parameter		Composition/wt.%		
	E_p/J	P_{AP}/kW	Al	Mg	Si
4	25.00	4.20	97.60	2.02	0.38
9	16.70	2.80	96.54	3.23	0.23

vapourisation of the element. Since the value is even below 2.62 wt.% originally contained in the base metal, it was believed that the reduction in Mg composition in the fusion zone is a result of vapourisation which is adjudged to have taken place during melting of the solid metals and solidification of the molten metals. Compared with the sample 4, the degree of the Mg vapourisation is lower in the sample 9. This can be attributed to the lower pulse energy and average peak power available during welding process.

3.3.3 XRD analysis

Figure 5 presents the XRD patterns of the top surface of the fusion zone of the two weld samples. The two spectra revealed the presence of aluminium (Al) and aluminium–iron–silicon ($Al_{0.5}Fe_3Si_{0.5}$) in the fusion zone. The peaks for these phases occurred at similar positions of 2θ .

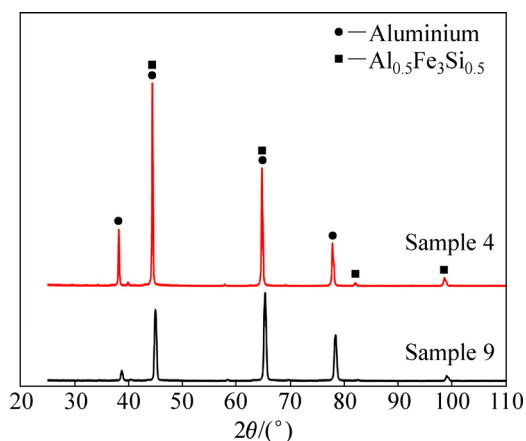


Fig. 5 XRD patterns of pulse laser weld joints of AA 5052-H3 alloy with ER 5356 aluminium filler metal

Following the SEM/EDX results presented in Table 5, the aluminium phase is adjudged to be the continuous dark phase marked ‘B’ in Fig. 4(c) because it contains 97.7 wt.% Al with no other element except Mg (2.3 wt.%). The aluminium iron silicon ($Al_{0.5}Fe_3Si_{0.5}$) phase is categorically identified as the white contrast angular phase because of the high Fe (19.24 wt.%) and trace quantity of Si (0.34 wt.%) in Al (79.6 wt.%). The formation of $Al_{0.5}Fe_3Si_{0.5}$ (intermetallic compound) in the fusion zone is due to the melting of the aluminium alloys (base metal and filler metal) which initiated chemical reactions between the constituent elements.

By comparing the XRD patterns shown in Fig. 5, the peaks for the $Al_{0.5}Fe_3Si_{0.5}$ are of higher intensity in the sample 4. The higher peak intensity suggests that there is increased formation of the intermetallic compound in the sample 4. This is probably due to more intense melting and slower solidification caused by higher P_{AP} and E_p during welding process. In the past, the formation of this hard intermetallic compound ($Al_{0.5}Fe_3Si_{0.5}$) was discovered in arc-welded AA 6061 using Al–Si as filler metal [29].

3.4 Microhardness

The microhardness profiles for weldment samples 4 and 9 are presented in Fig. 6. Indentations were made on each weldment from the base metal through the HAZ to the fusion zone. The test was performed on three samples cut from each of the two weldments. It is obvious that the hardness varied across the three zones. Generally, the base metal exhibits the lowest hardness value of (81 ± 2) $HV_{0.1}$ and (78 ± 1) $HV_{0.1}$ for the weldment samples 4 and 9, respectively. The value obtained is very close to the established hardness value (~ 72 HV) for AA 5052, as reported by EL-BATAHGY and KUTSUNA [16]. The slight change in value might be due to the manufacturing processes involved in the production of the AA 5052-H32 alloy.

The HAZ and fusion zone of the two samples exhibited higher and the highest hardness values, respectively. According to YUCE et al [13], this trend across the zones is due to grain refinement caused by

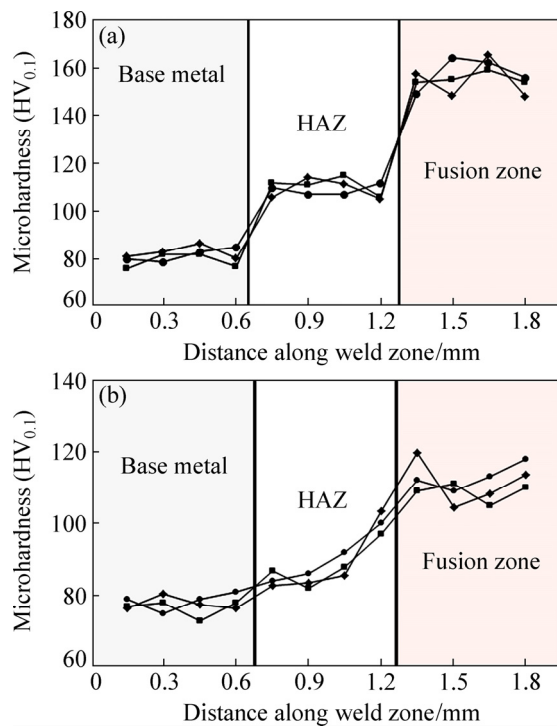


Fig. 6 Microhardness profiles across base metal, HAZ and fusion zone of AA 5052-H3 alloy: (a) Sample 4 formed at high E_p and P_{AP} ; (b) Sample 9 formed at low E_p and P_{AP}

rapid cooling rate occurring in the HAZ and fusion zones. In addition, the presence of the intermetallic compound ($Al_{0.5}Fe_3Si_{0.5}$) as confirmed by XRD analysis increased the hardness of the fusion zones. Compared with the weldment sample 9 which exhibited (89 ± 4) $HV_{0.1}$ and (111 ± 3) $HV_{0.1}$ in the HAZ and fusion zone, respectively, weldment sample 4 showed higher value of hardness in HAZ $((110 \pm 2)$ $HV_{0.1})$ and fusion zone $((156 \pm 4)$ $HV_{0.1})$. Though the sample 9 with lower E_p (16.7 J) and P_{AP} (2.8 kW) has better grain refinement, the higher hardness found at higher E_p (25 J) and P_{AP} (4.2 kW) indicates that the formation of the intermetallic compound ($Al_{0.5}Fe_3Si_{0.5}$) is higher in the sample 4. The increased formation of the harder compound enhanced the hardness of the weldment. This result agrees with the previous finding of CLARE et al [30].

3.5 Tensile strength

The results of the tensile test conducted on the base metal and the selected two weldments are presented in Fig. 7. Each result is an average of three measurements. The tensile strength of the as-received base metal is (230 ± 3.7) MPa while the two weldments showed lower tensile strength at break. Sample 9 has (168.1 ± 7.1) MPa whereas the lowest value of (143.9 ± 4.2) MPa was found for weld sample 4. However, the tensile strengths of the two selected weldments are much higher than those exhibited by other seven samples characterised with

solidification cracking. Weldment strength ratios (weld strength/parent metal strength) of 0.73 and 0.63 were found for sample 9 and sample 4, respectively. These are acceptable for Class C (non-critical structures) fusion weld joint applications in aerospace industry.

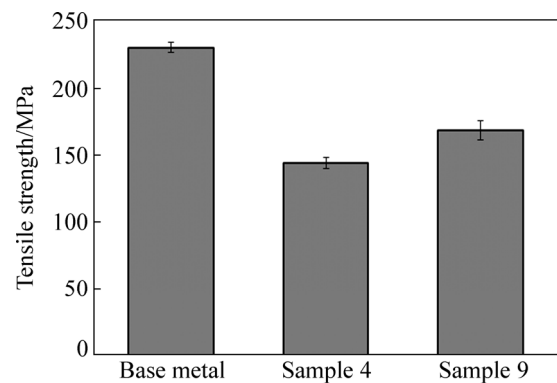


Fig. 7 Tensile strength of selected weld samples and base metal

Compared with the base metal, the lower strength exhibited by the two selected weldments can be traced to the different grain structures and hardness exhibited at the different zones of the weldments. Also, fracture ductility will be lower at the weld joint (fusion zone) because of the presence of the harder intermetallic compound (IMC). The presence of IMC ($Al_{0.5}Fe_3Si_{0.5}$) in the weld joint improved the weld hardness because of high hardness of the IMC. However, past researches have shown that weld joint ductility reduces with increased formation of IMCs because IMCs are brittle in nature and have high cracking propensity [31–33]. Formation of IMCs often results in volumetric increase in the melt pool and mismatch in properties (such as thermal expansivity, and thermal conductivity). These usually lead to lower tensile strength of the weldments because localised stress and strain are quickly built up at the point of mismatch in properties [34]. As reported by OKON et al [15], the depletion of the alloying elements (in this case, Mg) in the fusion zone would also have partly contributed to the loss of strength at the weld joint. The two selected weldments fractured at the weld joint, confirming that the area of weaker strength is the weld joint. The better strength of (168.1 ± 7.1) MPa exhibited by the weldment sample 9 is partly due to the finer grain structure and higher Mg content in its fusion zone, as compared to the sample 4 $((143.9 \pm 4.2)$ MPa). The reason is due to the lower E_p and P_{AP} resulting in lower Mg element vapourisation and faster cooling in the fusion and heat affected zones.

3.6 Fracture surface analysis

The surfaces of the fractured tensile specimens examined under a scanning electron microscope are shown in Fig. 8. Cup- and cone-like surface representing

dimple structures are found in all the examined fractured specimens. According to BOBBILI et al [35], the formation of dimple structure is an indication that the specimens undergo ductile fracture. Weld sample 9 is characterised with the co-existence of small and large dimples with significantly little existence of flat surface. However, it is obvious that the smaller dimples are of higher number density compared with larger dimples.

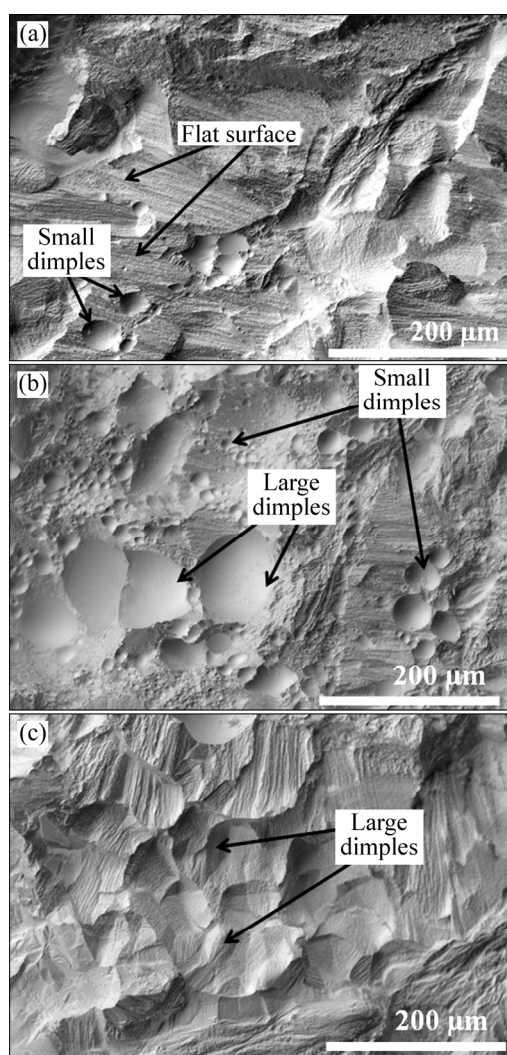


Fig. 8 SEM micrographs showing fracture surface after tensile test: (a) Weld sample 4; (b) Weld sample 9; (c) As-received base metal

As shown in Fig. 8, the weld sample 4 has the lowest number of dimples with the existence of nearly flat surfaces at some positions. The existence of the flat surface is an indication that brittle fracture occurred. This explains the lowest tensile strength found for weld sample 4 because brittle fracture is characterised with sudden failure of specimen during tensile test. The as-received AA 5052-H32 aluminium alloy specimen exhibited more large dimples and few existence of flat surface after fracture.

4 Conclusions

(1) Pulse laser welding of 0.6 mm-thick AA 5052-H32 alloy has been successfully performed. Appropriate parametric combinations that produced weld joints suitable for aircraft structures based on AWS D17.1 specification were obtained. The appropriate parametric combinations are (I) high pulse energy (25 J) and high average peak power (4.2 kW) and (II) low pulse energy (17.6 J) and low average peak power (2.8 kW).

(2) The weld width was found to increase with increasing the pulse laser current, pulse frequency and decreasing the pulse duration.

(3) The weld joints were characterised with the dendritic grain structure which became finer at low pulse energy and low average peak power (i.e. lower heat energy input). Loss of Mg which was more significant at higher heat energy input was observed in the weld joints. Hard phase intermetallic compound ($Al_{0.5}Fe_3Si_{0.5}$) was detected in the weld joints and its formation increased at higher heat energy input.

(4) Grain refinement occurrence and hard phase compound formation were responsible for the higher hardness exhibited at the weld joint compared with the base metal. Due to increased formation of the hard phase compound, the weld joint formed at higher energy input is harder ($(156\pm4) HV_{0.1}$) than the weld joint formed at lower heat energy input ($(111\pm3) HV_{0.1}$). However, lower tensile strength found at higher heat energy input was partly traced to reduced ductility of the weld joint due to increased presence of hard phase compound and increased Mg loss. The tensile strengths of the weldments which are 63% (at high energy) and 73% (at low energy) of the base metal (230 MPa) are acceptable for non-critical aircraft components.

Acknowledgments

The authors appreciate the funding (University-Industry Engagement Grant) and support provided by the Universiti Sains Malaysia under the Teaching Fellowship Scheme.

References

- [1] MANKARI K, ACHARYYA S G. Development of stress corrosion cracking resistant welds of 321 stainless steel by simple surface engineering [J]. *Applied Surface Science*, 2017, 426: 944–950.
- [2] GAO Xiao-long, LIU Jing, ZHANG Lin-jie. Dissimilar metal welding of Ti6Al4V and Inconel 718 through pulsed laser welding-induced eutectic reaction technology [J]. *The International Journal of Advanced Manufacturing Technology*, 2018, 96: 1061–1071.
- [3] WINDMANN M, RÖTTGER A, KÜGLER H, THEISEN W. Laser beam welding of magnesium to coated high-strength steel 22MnB₅

- [J]. *The International Journal of Advanced Manufacturing Technology*, 2016, 87: 3149–3156.
- [4] CAO Xin-jin, JAHAZI M, IMMARIGEON J P, WALLACE W. A review of laser welding techniques for magnesium alloys [J]. *Journal of Materials Processing Technology*, 2006, 171: 188–204.
- [5] DURSUN T, SOUTIS C. Recent developments in advanced aircraft aluminium alloys [J]. *Materials and Design*, 2014, 56: 862–871.
- [6] WU Yi-xiong, CAI Yan, WANG Huan, SHI Shao-jing, HUA Xue-ming. Investigation on microstructure and properties of dissimilar joint between SA553 and SUS304 made by laser welding with filler wire [J]. *Materials and Design*, 2015, 87: 567–578.
- [7] MOSTAAN H, SHAMANIAN M, HASANI S, SAFARI M, SZPUNAR J A. Nd:YAG laser micro-welding of ultra-thin FeCo–V magnetic alloy: Optimization of weld strength [J]. *Transactions of Nonferrous Metals Society of China*, 2017, 27: 1735–1746.
- [8] SONG C Y, PARK Y W, KIM H R, LEE K Y, LEE J. The use of Taguchi and approximation methods to optimize the laser hybrid welding of a 5052-H32 aluminium alloy plate [J]. *Journal of Engineering Manufacture, Proceedings of the Institution of Mechanical Engineers Part B*, 2008, 222: 507–517.
- [9] WANG Jing, WANG Hui-ping, WANG Xiao-jie, CUI Hai-chao, LU Feng-gui. Statistical analysis of process parameters to eliminate hot cracking of fiber laser welded aluminum alloy [J]. *Optics and Laser Technology*, 2015, 66: 15–21.
- [10] BAGHJARI S H, AKBARI MOUSAVI S A A. Effects of pulsed Nd:YAG laser welding parameters and subsequent post-weld heat treatment on microstructure and hardness of AISI 420 stainless steel [J]. *Materials and Design*, 2013, 43: 1–9.
- [11] ZHANG Xin-yi, YANG Wu-xiong, XIAO Rong-shi. Microstructure and mechanical properties of laser beam welded Al–Li alloy 2060 with Al–Mg filler wire [J]. *Materials and Design*, 2015, 88: 446–450.
- [12] SHANAVAS S, EDWIN RAJA DHAS J, MURUGAN N. Weldability of marine grade AA 5052 aluminum alloy by underwater friction stir welding [J]. *The International Journal of Advanced Manufacturing Technology*, 2018, 95: 4535–4546.
- [13] YUCE C, TUTAR M, KARPAT F, YAVUZ N, TEKIN G. Effect of process parameters on the microstructure and mechanical performance of fiber laser welded AA5182 aluminum alloys [J]. *Strojniški Vestnik–Journal of Mechanical Engineering*, 2017, 63: 510–518.
- [14] CHEN W, MOLIAN P. Dual-beam laser welding of ultra-thin AA 5052-H19 aluminum [J]. *International Journal of Advanced Manufacturing Technology*, 2008, 39: 889–897.
- [15] OKON P, DEARDEN G, WATKINS K, SHARP M, FRENCH P. Laser welding of aluminium alloy 5083 [C]//*Proceeding of 21st International Congress on Applications of Lasers and Electro-Optics*. Scottsdale, 2002: 1–10.
- [16] EL-BATAHGY A, KUTSUNA M. Laser beam welding of AA5052, AA5083, and AA6061 aluminum alloys [J]. *Advances in Materials Science and Engineering*, 2009, 2009: 1–9.
- [17] MALEK GHAINI F, SHEIKHI M, TORKAMANY M J, SABBAGHZADEH J. The relation between liquation and solidification cracks in pulsed laser welding of 2024 aluminium alloy [J]. *Materials Science and Engineering: A*, 2009, 519: 167–171.
- [18] SHEIKHI M, MALEK GHAINI F, ASSADI H. Prediction of solidification cracking in pulsed laser welding of 2024 aluminium alloy [J]. *Acta Materialia*, 2015, 82: 491–502.
- [19] ATABAKI M M, YAZDIAN N, KOVACEVIC R. Partial penetration laser-based welding of aluminum alloy (AA 5083-H32) [J]. *Optik–International Journal for Light and Electron Optics*, 2016, 127: 6782–6804.
- [20] BUNAZIV I, AKSELSEN O M, SALMINEN A, UNT A. Fiber laser-MIG hybrid welding of 5 mm 5083 aluminum alloy [J]. *Journal of Materials Processing Technology*, 2016, 233: 107–114.
- [21] SOKOLOV M, SALMINEN A, KUZNETSOV M, TSIBULSKIY I. Laser welding and weld hardness analysis of thick section S355 structural steel [J]. *Materials and Design*, 2011, 32: 5127–5131.
- [22] SU C, ZHOU J Z, YE Y X, HUANG S, MENG X K. Study on fiber laser welding of AA6061-t6 samples through numerical simulation and experiments [J]. *Procedia Engineering*, 2017, 174: 732–739.
- [23] WANG Xiao-jie, LU Feng-gui, WANG Hui-ping, QU Zhao-xia, XIA Li-qian. Micro-scale model based study of solidification cracking formation mechanism in Al fiber laser welds [J]. *Journal of Materials Processing Technology*, 2016, 231: 18–26.
- [24] MOHD HANAPI M H, ZUHAILAWATI H, ALMANAR I P, ANASYIDA A S. Optimization processing parameter of 6061-T6 alloy friction stir welded using Taguchi technique [J]. *Materials Science Forum*, 2016, 840: 294–298.
- [25] TZENG Y F. Parametric analysis of the pulsed Nd:YAG laser seam-welding process [J]. *Journal of Materials Processing Technology*, 2000, 102: 40–47.
- [26] CAM G, IPEKOGLU G. Recent developments in joining of aluminium alloys [J]. *International Journal of Advanced Manufacturing Technology*, 2017, 91: 1851–1866.
- [27] KOU S. *Welding metallurgy* [M]. 2nd ed. Hoboken, New Jersey: John Wiley and Sons Publishers, 2003.
- [28] ABIOYE T E, MEDRANO-TELLEZ A, FARAYIBI P K, OKE P K. Laser metal deposition of multi-track walls of 308LSi stainless steel [J]. *Materials and Manufacturing Processes*, 2017, 32: 1660–1666.
- [29] MIAO Yu-gang, ZHANG Ben-shun, WU Bin-tao, WANG Xiao-xiao, CHEN Guang-yu, HAN Duan-feng. Joint characteristics and corrosion properties of bypass-current double-sided arc-welded aluminum 6061 alloy with Al–Si filler metal [J]. *Acta Metallurgica Sinica (English Letters)*, 2016, 29: 360–366.
- [30] CLARE A T, OYELOLA O, ABIOYE T E, FARAYIBI P K. Laser cladding of rail steel with Co–Cr [J]. *Surface Engineering*, 2013, 29: 731–736.
- [31] KHOJASTEHNZHAD V M, POURASL H H. Microstructural characterization and mechanical properties of aluminum 6061-T6 plates welded with copper insert plate (Al/Cu/Al) using friction stir welding [J]. *Transactions of Nonferrous Metals Society of China*, 2018, 28: 415–426.
- [32] ABIOYE T E, FOLKES J, CLARE A T, MCCARTNEY D G. Concurrent Inconel 625 wire and WC powder laser cladding: Process stability and microstructural characterisation [J]. *Surface Engineering*, 2013, 29(9): 647–653.
- [33] XUE Jun-yu, LI Yuna-xing, CHEN Hui, ZHU Zong-tao. Wettability, microstructure and properties of 6061 aluminum alloy/304 stainless steel butt joint achieved by laser-metal inert-gas hybrid welding-brazing [J]. *Transactions of Nonferrous Metals Society of China*, 2018, 28: 1938–1946.
- [34] OGEDENGBE T I, ABIOYE T E, EKPEMOGU A I. Investigation of mechanical properties and parametric optimization of the dissimilar GTAW of AISI 304 stainless steel and low carbon steel [J]. *World Journal of Engineering*, 2018, 15(5): 584–591.
- [35] BOBBILI R, MADHU V, GOGIA A K. Tensile behaviour of aluminium 7017 alloy at various temperatures and strain rates [J]. *Journal of Materials Research and Technology*, 2016, 5: 190–197.

航空航天用脉冲激光焊接 5052-H32 铝合金薄板的外观、显微组织和力学性能

T. E. ABIOYE^{1,2}, H. ZUHAILAWATI¹, S. AIZAD¹, A. S. ANASYIDA¹

1. Structural Materials Niche Area, School of Materials and Mineral Resources Engineering, Engineering Campus, Universiti Sains Malaysia, 14300 Nibong Tebal, Penang, Malaysia;
2. Industrial and Production Engineering Department, School of Engineering and Engineering Technology, Federal University of Technology Akure, PMB 704, Akure, Ondo State, Nigeria

摘要: 制备 0.6 mm 厚的 AA5052-H32 铝合金薄板, 研究符合航空航天工业 AWS D17.1 规范的脉冲激光焊接工艺的最佳参数, 如激光脉冲电流、脉冲频率和脉冲持续时间。研究焊缝的显微组织和力学性能, 确定参数与焊缝几何形状的关系。在高脉冲能量(25 J)、高平均峰值功率(4.2 kW)和低脉冲能量(17.6 J)、低平均峰值功率(2.8 kW)两种条件下可获得满足 AWS D17.1 要求的无凝固裂纹的优质焊缝。在较低热量输入下形成的焊缝具有更细小的枝晶结构, 且焊缝中 Mg 的蒸发和硬质相化合物($Al_{0.5}Fe_3Si_{0.5}$)的形成减少。因此, 与在较高热量输入下形成的焊件相比, 在较低热量输入下形成的焊件的抗拉强度(168 MPa)提高 1.15 倍, 但其接头处的硬度(111 HV_{0.1})下降约 29%。总之, 为了获得满足 AWS D17.1 要求的 0.6 mm 厚 AA5052-H32 脉冲激光焊接接头, 选择合适的参数至关重要。

关键词: 脉冲激光焊接; 铝合金; 薄板; 显微组织; 力学性能; 凝固裂纹; 金属间化合物

(Edited by Bing YANG)